

OPEN

# Photodynamic effect of Zirconium phosphate biocompatible nano-bilayers containing methylene blue on cancer and normal cells

Reza Hosseinzadeh<sup>1</sup> & Khatereh Khorsandi<sup>2</sup>

Pharmaceutical applications of methylene blue, especially as photosensitizer, have been limited due to its rapid enzymatic reduction in the biological systems. In this study nano-platelet zirconium phosphate was synthesized and its biocompatibility was evaluated. The synthesized material was considered as drug delivery vehicle for methylene blue to enhance the photodynamic therapy efficacy in human breast cancer cells. Zirconium phosphate-methylene blue nano-hybrids were characterized by X-Ray Powder Diffraction (XRPD), Scanning Electron Microscopy (SEM), and Thermo gravimetric Analysis (TGA). Biocompatibility of synthesized nano materials were studied on Hu02 human fibroblast normal cell and MDA-MB-231 human breast cancer cell. The results clarified that ZrP-MB nanoparticles could decrease the dark toxicity of free methylene blue. Photodynamic therapy using zirconium phosphate-methylene blue on MDA-MB-231 human breast cancer was evaluated by MTT assay, colony forming ability assay, AO/EB dual staining and flow cytometry detection of apoptosis. The results suggest that zirconium phosphate-methylene blue nano-hybrids significantly enhance photodynamic therapy efficacy probably via apoptosis cell death mechanism against human breast cancer cells. According to the results, zirconium phosphate nanoparticles could be suggested as a promising nano-carrier for photosensitizer delivery in photodynamic therapy.

Cancer is still one of the most challenging diseases and is the major cause of death after cardiovascular diseases. Breast cancer is one of the most common malignancies in women and second lethal cancer after lung cancer among females<sup>1-4</sup>. With development of knowledge about cancer diseases, many advances have been made to treat it<sup>2,3,5</sup>. Chemotherapy is one of major therapy methods and remains as common important tools in the metastatic breast cancer treatment<sup>6-13</sup>. Toxic effects of anticancer drugs on normal cells are still an important issue because they often act nonspecific<sup>14-16</sup>. Over the past two decades, new drug delivery systems have been developed that can overcome chemotherapy problems<sup>17-20</sup>. In recent years, more attention has been paid to the provision of nanoparticles as carriers for drug delivery. Nanoparticle carriers improve the function of drugs and reduce their side effects by changing the pharmacokinetic properties<sup>21,22</sup>. For synthesis of nanoparticles, various materials such as polymers, metal particles, lipids, etc. could be used which produce different shapes and sizes of nanoparticles. These structures have ability to control the release of drug, protection of drug molecule, particle size smaller than cells, cross biological barriers for reaching to the target site, increasing drug shelf life in the bloodstream, targeted drug delivery and biocompatibility which could be consider as highly effective delivery systems to increasing therapeutic efficacy of the drugs<sup>23-26</sup>. Recently, the use of inorganic nanomaterials for biomedical applications has been grown compared to traditional polymeric drug delivery systems. Among the variety of nanoparticles, inorganic layered compounds have a special interest in researches due to their high ion exchange capacity, crystalline structure, tunable particle size, non-spherical shapes and biocompatibility<sup>27-30</sup>.

Non-spherical inorganic layered structured nanomaterials (LSNs) are used in various research. There are many scientific reports on the applications of LSNs<sup>31</sup>. Among them, the zirconium phosphate layered cation exchange materials have been widely used in biomedical applications as drug vehicles because of their harmlessness to humans and not to interfere with the metabolic function of the body<sup>32</sup>. The size of synthesized ZrP

<sup>1</sup>Department of Medical Laser, Medical Laser Research Center, Yara Institute, ACECR, Tehran, Iran. <sup>2</sup>Department of Photodynamic, Medical Laser Research Center, Yara Institute, ACECR, Tehran, Iran. Correspondence and requests for materials should be addressed to R.H. (email: [r.hoseinzadeh@ut.ac.ir](mailto:r.hoseinzadeh@ut.ac.ir)) or K.K. (email: [khorsandi.kh@ut.ac.ir](mailto:khorsandi.kh@ut.ac.ir))

materials can be easily controlled by synthesis and modification methods. They should show better binding properties, cell adhesion and margination than spherical nanoparticles due to platelet-like shape of zirconium phosphate nano-structures<sup>33</sup>. ZrP can intercalate wide variety of drugs and due to ion exchange ability; it can release the interacted drugs in the acidic conditions such as cancer cells microenvironment<sup>34–36</sup>. The lysosome and the peroxisomes could dissociate zirconium phosphate to phosphate ions and harmless zirconium salts<sup>34</sup>. In addition, good biocompatibility, bioactivity, cheap availability, simple synthesis method and high stability of zirconium phosphate provides the potential for their use in biomedical. Nowadays, these materials are very attractive nano-carriers for delivery of drugs, proteins, and genes<sup>32,34</sup>.

Photodynamic therapy (PDT) is a non-invasive radiation therapy which use for treatment of types of cancers, cardiovascular and ophthalmic diseases. PDT is based on photo activation of light sensitive material (photosensitizer). The activated photosensitizers transfer their excess energy to the surrounding oxygen to form the reactive oxygen species (ROS), particularly singlet oxygen as cytotoxic reactive materials, which will cause damage in cancer cells and tissues<sup>4,37–39</sup>. Another great advantage of PDT is its potential on overcoming multidrug resistance (MDR) due to specific cytotoxicity mechanism of photosensitizers onto cancer cells which is different from chemotherapy agent's mechanisms<sup>40–42</sup>. The significant side effects of photosensitizer are nonspecific interactions and damage to normal cells and tissues due to low selectivity to specific cells, environmental photosensitizer degradation and water insolubility or molecular hydrophobicity which cause various limitations in clinical application of photodynamic therapy<sup>4,39</sup>. Application of nanoparticles in photosensitizer delivery to tumor cells in PDT has been improved. Advantages such as stable aqueous dispersion of hydrophobic photosensitizers, surface modification ability, targeted therapy, protecting photosensitizers from environmental degradation and quenching can be achieved by using nano-delivery systems<sup>43</sup>. According to the chemical and redox properties of methylene blue (MB), the clinical use of MB has been hindered due to simple reduction of MB to photodynamic inactive reduced form “leuco-methylene blue” in biological systems. The two major reducing systems accompanied with inactivating of methylene blue are the presence of a transmembrane thiazine dye reductase at the cell surface and intercellular reduction by NADH/NADPH dehydrogenases<sup>44</sup>. In this study, we have synthesized and characterized zirconium phosphate layered nano-sheets and used them as methylene blue nano-carriers for photodynamic therapy of human breast cancer cells. The loaded amounts of MB were determined by spectrophotometric and thermal methods and *in vitro* release of the drug from nano-delivery system was evaluated. *In vitro* cytotoxicity and death mechanism of ZrP-MB nanoparticles on photodynamic treatment of MDA-MB-231 human breast cancer cell line was determined.

## Materials and Methods

Zirconyl chloride ( $\text{ZrOCl}_2 \cdot 8\text{H}_2\text{O}$ ), phosphoric acid and Methylene blue were obtained from Merck. DMEM medium (Dulbecco's Modified Eagle Medium) was purchased from Invitrogen. MTT assay reagent, (3-(4,5-dimethylthiazol-2-yl)-2,5-diphenyltetrazolium bromide), was supplied by Sigma-Aldrich. Trypan blue solution (0.4% w/v) and dimethyl sulfoxide (DMSO) were achieved from Merck Company. Fetal bovine serum (FBS) and antibiotics were purchased from Gibco (Gibco BRL). All chemicals were of analytical grade. Double distilled deionized water was used for all experiments and solutions. All pH measurements were made at 25 °C using Bel PHS3-BW (BEL ENGINEERING, Italy). The UV-Vis absorption spectra were recorded using Cary 60 UV/Vis spectrophotometer, equipped with quartz cells. Red light emitting LED (660 nm; power density: 30 mW cm<sup>-2</sup>) was used as light source for photodynamic experiments.

**Synthesis of zirconium phosphate.** Synthesis of Zirconium phosphate was done based on procedures reported previously in literatures<sup>45,46</sup>. Briefly, a certain amount of Zirconyl chloride octahydrate was dissolved in deionized water (14 mM) and stirred vigorously until complete dissolution. The resulting homogeneous solution was added dropwise to a diluted phosphoric acid solution (28 mM) and vigorously stirred. The pasty precipitate was produced. The resulting mixture was transferred to the sealed teflon-lined stainless steel autoclave. The autoclave was kept at 180–200 °C for 9 h and then cool down to room temperature under ambient conditions. The synthesized products were collected by centrifugation. For removing other contaminants from final product, the collected precipitate was re-suspended in deionized water and collected by centrifugation for three times.

**Characterization of synthesized zirconium phosphate.** Characterization of the synthesized materials was done using several analytical methods. the crystal structure of ZrP was characterized using X-Ray powder diffraction analysis. XRD patterns were obtained by a Rigaku MiniFlex X-ray diffractometer using  $\text{CuK}\alpha$  radiation ( $\lambda = 0.154 \text{ nm}$ ). The divergence, receiver, and detector slits width were 2 mm; the scatter slit width was 0.6 mm. SEM images were obtained using scanning electron microscope for powder samples by Zeiss SEM instrument (Zeiss EVO-18, Germany). EVO 18 offers Energy and Wavelength Dispersive Spectroscopy (EDS & WDS) for surface elemental analysis. The Specific Surface Area (SSA) obtained and calculated for synthesized nanoparticles (65.8 m<sup>2</sup>/g). Fluorescence spectra was recorded by Cary Eclipse fluorescence spectrophotometer equipped with a thermostatically controlled cell holder at ambient temperature. The excitation and emission slits were set at 5 nm. Cary 100 UV-vis spectrophotometer, equipped with quartz cuvettes was used for recording UV-Vis absorption spectra.

**Methylene blue intercalation in layered zirconium phosphate.** Methylene blue was intercalated into zirconium phosphate layers according to previous methods<sup>32</sup>. The certain amount of zirconium phosphate suspended in the solutions contains constant concentrations of methylene blue. The experimental suspensions are kept in dark and shaken continuously. The absorbance of centrifuged samples supernatant was measured in 30 minutes' time intervals until reaching to constant value as indicative of the end of methylene blue intercalation. The optimum time concerned with intercalation process obtained by continuous measurements of methylene

blue absorbance in the supernatants at various times to obtaining intercalation equilibrium time. After reaching the intercalation equilibrium, the suspension was centrifuged and supernatant discarded. The obtained precipitate washed three times for removing excess free MB (un-intercalated MB) from intercalation materials.

**Thermo gravimetric analysis (TGA).** Thermal gravity analysis was recorded using STA 1500, from Rheometric Scientific Co. The percentage of loaded methylene blue into ZrP nanoparticles was calculated by thermo gravimetric analysis. The thermal weight losses were recorded by increasing of temperature up to 600 °C by the ramp of 5 °C/min.

**Cellular experiments.** Human normal fibroblast cells (HU02) and human breast cancer cells (MDA-MB-231) were purchased from the Institute of Pasture, Tehran, Iran. DMEM medium supplemented with 10% FBS, 100 IU/ml penicillin, and 100 mg/ml of streptomycin was used as cell culture medium. The cells were grown in the supplied medium and then incubated in a humidified incubator containing 5% CO<sub>2</sub> at 37 °C. The cells were removed by trypsinizing (trypsin 0.025%, EDTA 0.02%) and washed with phosphate buffer solution and then cultured for experimental purposes. For treatments, the MB and ZrP-MB solutions prepared freshly using PBS buffer solution.

**MTT assay.** Colorimetric MTT (Thiazolyl blue tetrazolium bromide) assay was used for cell viability evaluation. Living cells convert the MTT to an insoluble formazan. The resulting formazan solubilized using dimethyl sulfoxide (DMSO) and its concentration measured using ELISA reader. Briefly, culture medium was removed and cells were incubated in medium containing 0.5 mg/mL of 3-(4,5-Dimethylthiazol-2-yl)-2,5-Diphenyltetrazolium bromide for 4 h at 37 °C. The resulting purple formazan crystals dissolved in 100 µL DMSO and shaken for 15 min. The absorbance of solutions was measured at 570 nm by an ELISA reader (Hyperion, Inc., FL, USA).

**Photodynamic experiments.** The MDA-MB-231 human breast cancer cells were grown in medium culture and after reaching 80~90% confluence the cells were washed with PBS, afterwards detached from the flask by addition of 1.0 mL of 0.25% trypsin for 1–3 min at 37 °C. Cells ( $1 \times 10^4$  cells/well) were seeded into 96-well plates. The cells were treated with analyts at different conditions. After a further incubation 1 h, one plate was considered as dark (no irradiation/control plate) and the other plates illuminated by Laser light (PDT). The MTT assay was used to determine the cell viability.

**Clonogenic cell survival assay.** Clonogenic cell survival assay was used for evaluation of the long-term proliferative potential of MDA-MB-231 cancer cells following PDT treatment. For this purpose, the treated cells were seeded at a density of 200 cells per well in 6-well plates and cultured for 7 days. Then, the media was removed from each plate and stained by 0.5% crystal violet in methanol<sup>47</sup>. The assay was done in triplicate.

**Determination of apoptosis by fluorescence microscopy and flow cytometry.** MDA-MB-231 cells were treated with 0, 10, and 50 µg/mL ZrP-MB for 1 h and then illuminated (PDT). the cells were washed with PBS and then were dissociated by trypsinization, collected by centrifugation at room temperature, and washed twice with PBS. Morphological changes due to apoptosis induction by photodynamic therapy mediated ZrP-MB were detected by Acridine Orange/Ethidium Bromide (AO/EB) double staining using fluorescence microscopy (BEL, Italy) according to previous procedures<sup>48–50</sup>. All samples were stained and analyzed immediately at room temperature. For quantitative analysis of apoptosis induction by photodynamic treatment mediated ZrP-MB, the cells were collected as described above and then were suspended in 500 µL binding buffer containing 5 µL FITC Annexin-V and 5 µL PI reagents. Cells incubated for 15 min in dark condition and room temperature, and then were analyzed using flow cytometer (FACS Calibur, USA).

**ROS detection.** Quantitation of ROS generated by MB and ZrP-MB in cells was performed by 2',7'-dichlorodihydrofluorescein diacetate (DCFH-DA, Sigma-D6883). DCFH-DA passes easily through the cell membrane where it is deacetylated to a non-fluorescent dihydrofluorescein, and an increase in fluorescence signal can be observed upon its oxidation. After PDT, the cells were trypsinized and, DCFH-DA was added to the medium at a final concentration of 2 mM. The plates were incubated for 45 minutes in the dark (37 °C, 5% CO<sub>2</sub>). Then medium containing DCFH-DA was removed and washed twice with PBS. The fluorescence emission of ROS can be detected by using excitation at 488 nm (blue) and emission at 530 nm (green) wavelengths. The generation of ROS was analyzed by Becton-Dickinson FACS Calibur Flow Cytometer (USA) using flowJo 7.6.1 software.

**Statistical analysis.** All values are expressed as means ± SD. Results are expressed as with *n* denoting the number of experiments.  $P < 0.05$  (\*) was considered as statistically significant.

**Ethical approval.** We didn't perform any human or animal tests. So our work does not need any ethical approve for experiments.

## Results and Discussion

**Synthesis, intercalation and characterization of nanoparticles.** Synthesized nanoparticle was used for intercalating of methylene blue based on cation exchange potential of zirconium phosphate bilayer nanostructures. Since the methylene blue is a small cationic thiazine dye (methylthionium chloride), in the presence of cation exchange material such as ZrP, the cationic dye exchange with interlayer H<sup>+</sup>. When the concentration of dye cation is high in solution, according to the thermodynamic rules, the chemical potential of dye in the bulk solution (and its related Gibbs free energy) is higher than intercalated dye. Due to the nature of spontaneous reactions; dye intercalated in the ZrP bilayers for decreasing Gibbs free energy of solution until the exchange

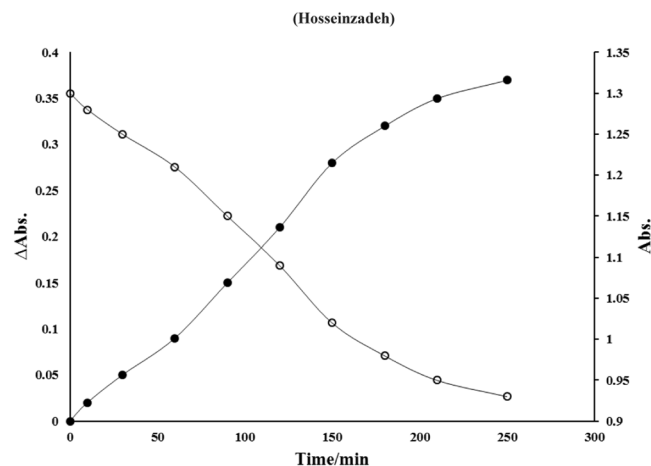


**Figure 1.** Alteration of methylene blue bulk Abs (○) and related ΔAbs (●) versus time (minute).

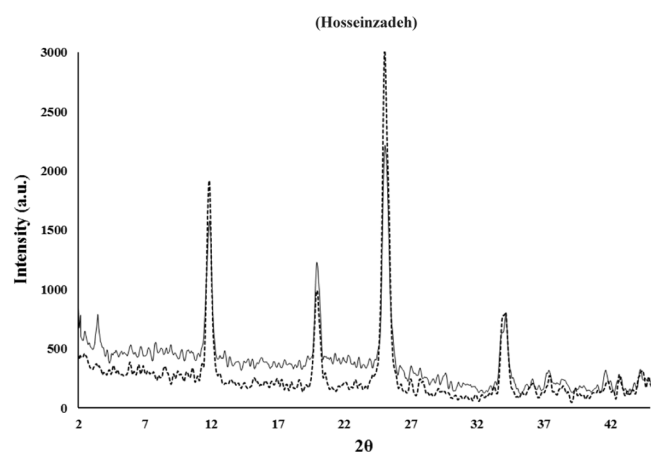


**Figure 2.** X-ray diffraction patterns of ZrP (—) and ZrP-MB (---) nanoparticles.

equilibrium reach. Figure 1, represents the dye absorbance ( $\lambda_{\max} = 664 \text{ nm}$ ) variations at different time intervals of ZrP-MB incubation at  $25^\circ\text{C}$  and  $\text{pH} = 7.4$ .

The absorbance was decreased by increasing incubation time until the equilibrium reaches. After equilibrium, the absorbance didn't show any significant changes. The bare and intercalated nanoparticles were characterized using various techniques. Figure 2 shows the XRD pattern of synthesized nanoparticles.

According to the previous reports, appeared peaks in plans 002 at ( $2\theta = 11\text{--}12$  (/degree), 110 at ( $2\theta = 19\text{--}20$  (/degree) and 112 at ( $2\theta = 24\text{--}26$  (/degree) are the characteristics peaks in  $\alpha$ -ZrP crystalline structure and no other impurity peaks were detected. (002) diffraction plane could be used for determination of the interlayer distances using the Bragg's Law for diffraction pattern of zirconium phosphate, and the (001) diffraction plane is useful for approving and determination of the intercalation products and composite interlayer distance<sup>33,51</sup>. Based on the Bragg equation;

$$d = \frac{\lambda}{2 \sin\theta}$$

The distance between planes ( $d$ ) is equal to the ratio of the  $\lambda$  (wavelength of the source) and  $2\sin(\theta)$ ; the diffraction angle). So, by using this equation, related parameters for synthesized materials can be determined. As mentioned above the 002 peak ( $2\theta \approx 12$ ) can be used for calculation of distance between layers of the ZrP (0.76 nm). Appearance of new peaks without any significant difference in the ZrP pattern approved the intercalation of methylene blue between interlayer of ZrP. As mentioned previously, the (001) diffraction plane was used for determination of the intercalation products and interlayer distance based on Bragg Law, (the obtained value is  $\approx 14\text{--}17 \text{ \AA}$ ). This expanding between ZrP crystalline sheets, demonstrated that methylene blue is injected into the interlayer distance. By considering the approximate dimensional parameters of methylene blue as 1.25–1.60 nm length, 0.57–0.84 nm width and thickness of about 0.5 nm, it seems that MB is intercalated longitudinally from top to bottom within the two sheet of ZrP by interaction of amine groups of MB with phosphate anions in the sheets (electrostatic interactions)<sup>52</sup>. According to the XRD pattern of intercalated into MB-ZrP, the pattern did

(Hosseinzadeh)

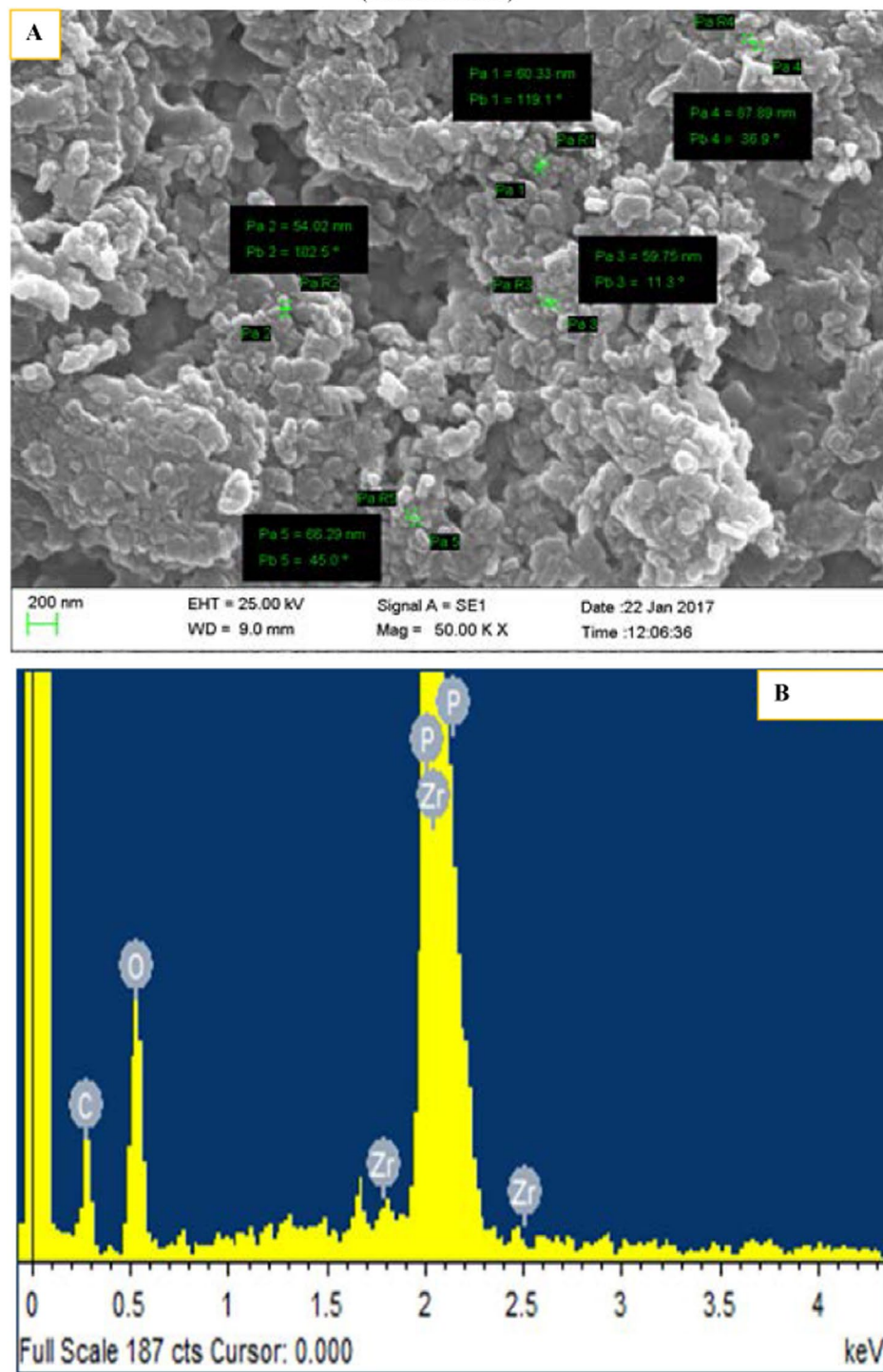


**Figure 3.** SEM image (A) and related EDS spectrum (B) of ZrP-MB nanoparticles.

not show any significant difference compared to pure ZrP nanocrystals indicating that ZrP remained unchanged during intercalation of methylene blue into the interlayer distance. The interlayer distance in  $\alpha$ -ZrP crystalline structure is about 7.6 Å where 1 Å occupied with interstitial water molecules in the interlayer gallery<sup>32</sup>. A new diffraction peak ( $2\theta \approx 4$ ) is presented in the methylene blue intercalated zirconium phosphate that demonstrated the intercalation of methylene blue into the interlayer distance of ZrP<sup>32</sup>. The size and morphology of the synthesized nanostructures were determined using scanning electron microscopy (SEM). Also, energy-dispersive X-ray spectroscopy (EDS) analysis was carried out on a scanning electron microscope. SEM images and EDS graphs were shown in Fig. 3.



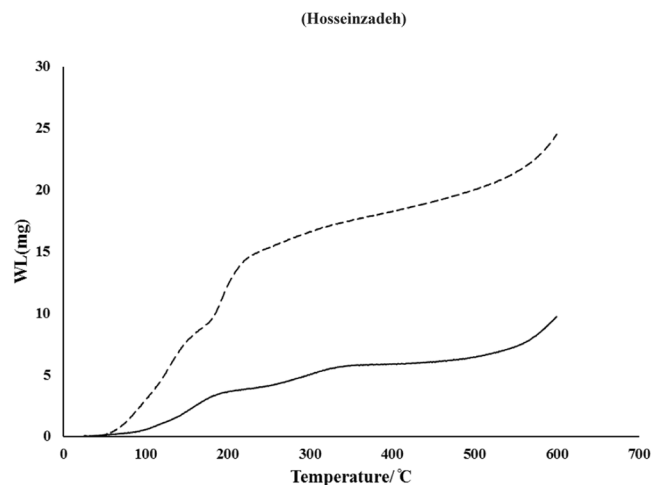


**Figure 4.** Thermogravimetric analysis (TGA) of ZrP (—) and the ZrP-MB (---).

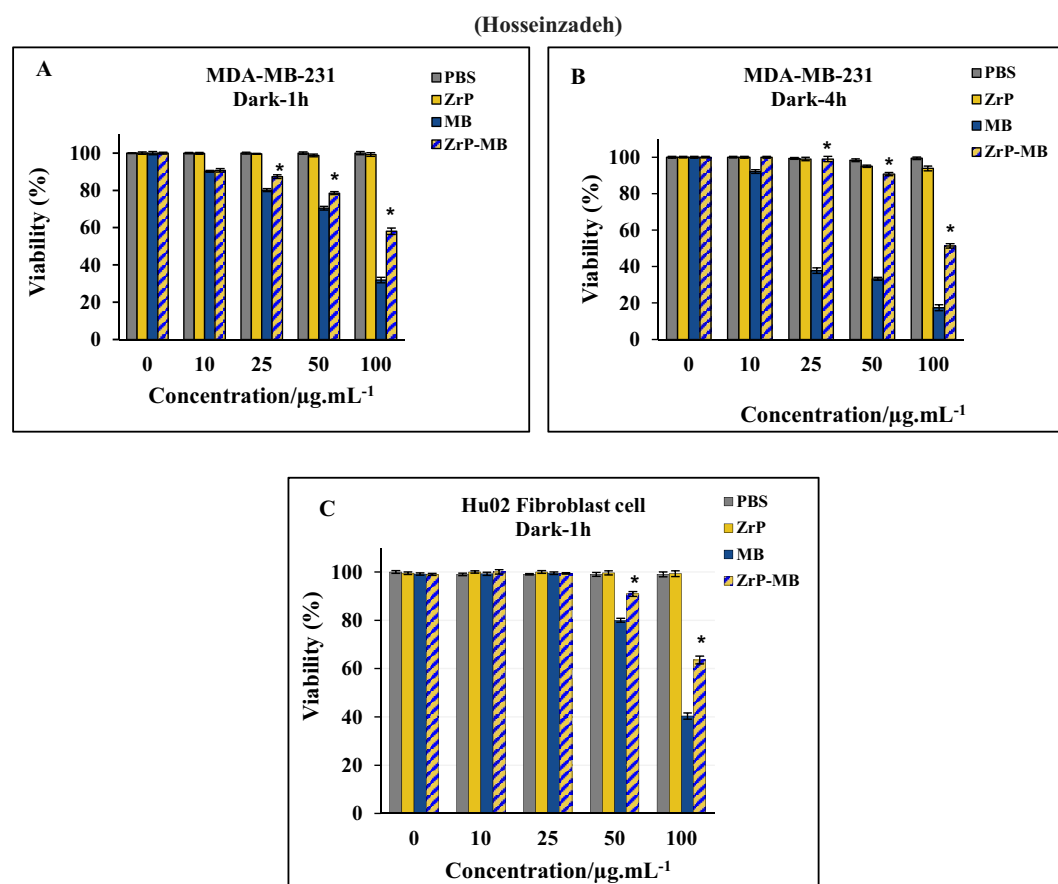


**Figure 5.** *In vitro* dark-toxicity of different concentrations of MB, based on MB contents, in ZrP-MB, ZrP, free MB and related blank (PBS) on MDA-MB-231 (A, 1 h incubation), MDA-MB-231 (B, 4 h incubation) and fibroblast HuO2 (C, 1 h incubation) cells, without laser irradiation. The results are expressed as mean  $\pm$  SD (n = 3), \* $P$  < 0.05 (compared with MB treated group).

The Fig. 3A shows uniform hexagonal morphology and layered structure with particle sizes ranging from 50 to 100 nm. Energy-dispersive X-ray spectroscopy analysis results (Fig. 3B), shows the Zr, O, P and C elements were incorporated into the system. The Zr, O, P and C elements homogeneously distributed throughout the prepared nanostructures. Figure 4 represents the thermal gravity (TG) graphs related to void ZrP and methylene blue intercalated ZrP.

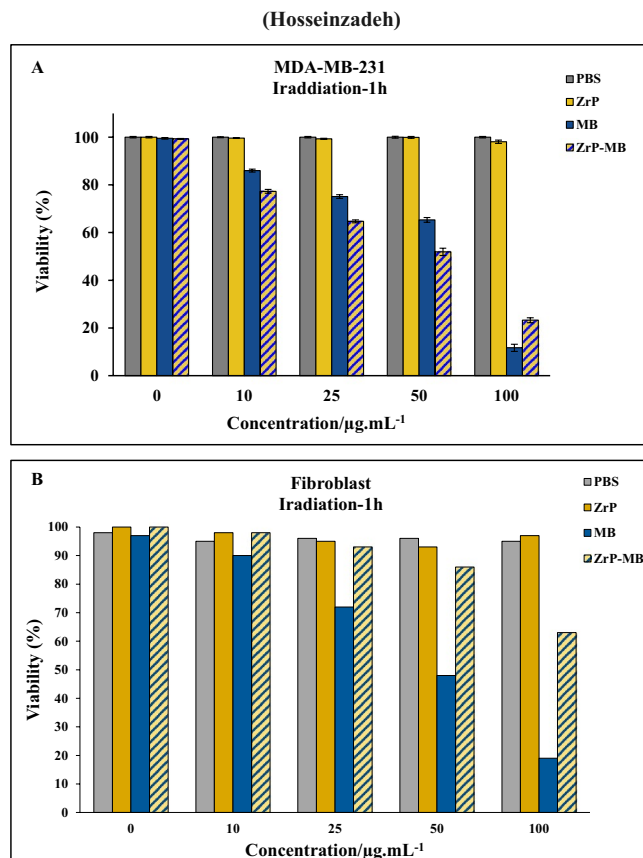


**Figure 6.** *In vitro* phototoxicity (laser irradiation) of different concentration of ZrP-MB, ZrP, MB and related blank (PBS) on MDA-MB-231 (A) and Fibroblast (B) cells after 1 h incubation. The results are expressed as mean  $\pm$  SD ( $n = 3$ ),  $*P < 0.05$  (compared with MB treated group).

Thermal gravity analysis (TGA) showed that methylene blue intercalated into the Zirconium phosphate nanolayers and maximum 30–35% loading was achieved. 30% loading in synthesized nanoparticles considered in further experiments. These results are in agreement with obtained results from spectrophotometric and EDS measurements.

**Biocompatibility of ZrP nanoparticles and *in vitro* cytotoxicity of ZrP-MB.** The effect of the zirconium phosphate nanomaterials on cell survival and cell proliferation was determined using MTT assay on MDA-MB-231 human breast cancer and human normal fibroblast cell lines. As reported previously, the incubation time can affect the dark toxicity of methylene blue, Santos *et al.*, reported that the dark toxicity of methylene blue increased by increasing the incubation time (more than 1 hour) at low MB concentrations in MCF-10A, MCF-7 and MDA-MB-231 cells, but at higher concentration of MB, dark toxicity of MB on MCF-10A and MCF-7 cells increased at short incubation times, but has little effect on MDA-MB-231 cell viability in similar incubation times<sup>53</sup>. To obtain the dark cytotoxicity of methylene blue and hybrid nanomaterials, the MDA-MB-231 cells were treated with different concentrations of MB, ZrP-NPs and ZrP-MB (concentration is shown in Fig. 5A,B) for 1 and 4 h incubation times, respectively. As it can be seen, the void ZrP nanoparticles did not change the cell viability upon changing the incubation time which shows the biocompatibility of ZrP nanoparticles. According to the results the MB dark toxicity is increased upon increasing the concentration of MB (more than 10  $\mu\text{g/mL}$ ) and incubation time more than 1 hour didn't show any significant effect on cell viability. It is clear that the dark toxicity of MB is decreased by using ZrP as drug delivery system and treating cell with ZrP-MB decreased the dark toxicity compared to free MB in dark condition. For analyzing the effect of MB and ZrP-MB on normal cells, we used the human normal fibroblast. As it can be seen in Fig. 5C, the cell viability did not change significantly in low concentration of treating materials up to 25  $\mu\text{g/mL}$  and by increasing the concentration (50  $\mu\text{g/mL}$  and 100  $\mu\text{g/mL}$ ) the cell viability decreased. According to the results, the dark toxicity of MB on normal cells is decreased by using ZrP-MB instead of MB. It can be suggested that this nano-system can reduce the dark toxicity of methylene blue in comparison with free methylene blue. This effect lead to selective and localized PDT mediated MB in cancer and tumor sites by illuminating laser light and inducing controllable cell killing.

**Laser irradiation effect on cytotoxicity of hybrid nanomaterials (*In vitro* photodynamic assay).** The effect of 660 nm laser light illumination (PDT) on ZrP-MB treated MDA-MB-231 cells (1 hour incubation) can be seen in Fig. 6A.

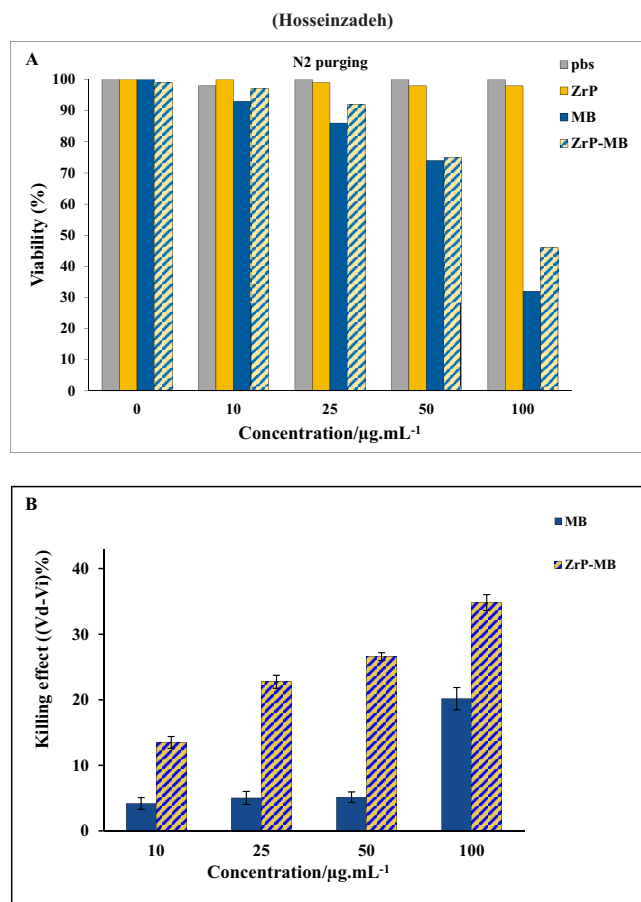


**Figure 7.** (A) Photodynamic activity of materials under N<sub>2</sub> inert gas purging for examination of O<sub>2</sub> effect. (B) Cell Viability (%) difference ( $V_{\text{Dark}} - V_{\text{Irradiation}}$ ) between dark and laser irradiation experiment for ZrP-MB, ZrP, MB treatments and related blank (PBS) on MDA-MB-231 cells, the results are expressed as mean  $\pm$  SD (n = 3), \* $P < 0.05$  (compared with MB treated group).

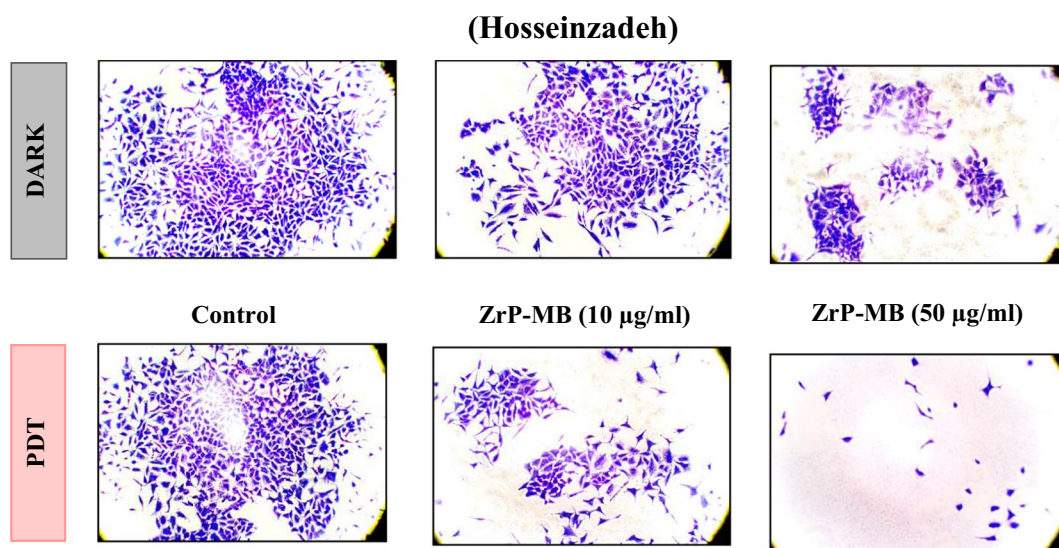


**Figure 8.** Clonogenic ability images (10X) of breast cancer cells at 0, 10 and 50 µg/mL of ZrP-MB at dark (control) and irradiation.



(Hosseinzadeh)

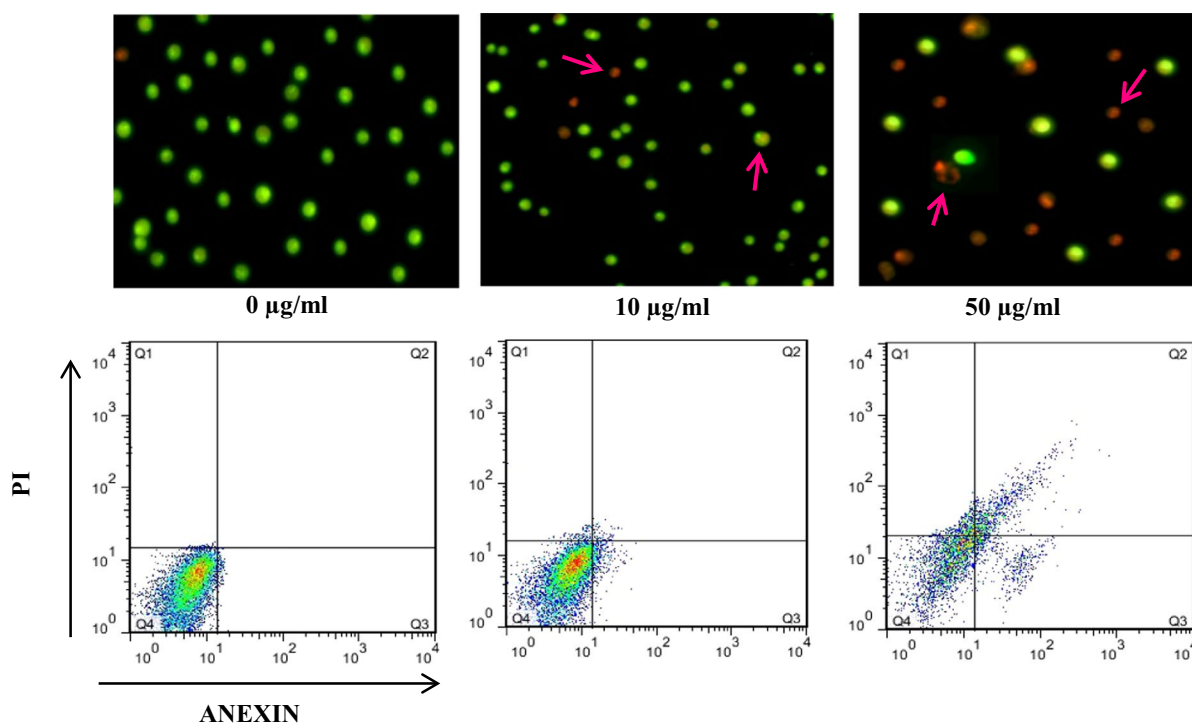


**Figure 9.** Apoptosis induction in MDA-MB-231 cells at 0, 10 and 50 µg/mL of ZrP-MB treatment under laser light irradiation using Acridine Orange (AO) and Ethidium Bromide (EB) double staining followed by fluorescence microscopy(40X) and annexin V-FITC and PI staining followed by flow cytometry. Arrows indicate apoptotic and necrotic cells.

The results show that in the presence of laser irradiation the cell viability in control (only PBS) didn't show any significant changes approve that the used dosage of light doesn't show any photo-toxicity in the absence of photosensitizers. Also, ZrP treated cells didn't show any significant changes in cell viability which approved the biocompatibility of synthesized layered ZrP nanostructures. The cell viability decreased by increasing photosensitizer (MB and ZrP-MB). In the presence of high concentrations of ZrP-MB and MB (100 µg/ml), cell viability decreased more in treated cells with MB than ZrP-MB. Interestingly, at lower concentrations of ZrP-MB and MB (lower than 100 µg/ml) the cell viability decreased more in treated cell with ZrP-MB than MB. In other words, the results demonstrated that photodynamic efficacy of ZrP intercalated MB is higher than free MB (Fig. 5).

Figure 6B represents the effect of various concentrations of materials on the fibroblast normal cells under red light illumination. Due to the incubation time after treatment, the normal cells can repair the damage and can normalized the oxidative stress on the cells. As reported previously, due to the function of mitochondria in normal cells, the induced ROS materials can scavenged by antioxidant enzymes, such as superoxide dismutase, H<sub>2</sub>O<sub>2</sub>-removing enzymes, catalase, peroxidases, metal binding proteins, in the normal cells mitochondrial system due to the redox signaling activation<sup>54-56</sup>. However, in cancer cells dysfunction of mitochondrial system caused to increasing ROS materials in the cancer cells without scavenging of reactive oxygen species, because of inactivation of redox signaling in the cancer cells due to mitochondrial dysfunction. So normal cells can repair themselves by activation of antioxidant ROS scavenging bio system but cancer cells don't have this ability. Also it must be mentioned that the selective irradiation can decrease the damage to normal cells. By considering the cancerous parts as the targeting points for laser irradiation, the normal cell damages can be controlled and decreases<sup>57-59</sup>. Figure 7 depicted the molecular oxygen effect on PDT activity of treating materials (Fig. 7A) and photodynamic effect on cancer cells, after subtracting the dark toxicity for each treatment (Fig. 7B).

**Clonogenic cell survival assay.** A Clonogenic cell survival assay was performed to evaluate the long term proliferative potential of MDA-MB-231 cells after PDT treatment. This assay used for determination of the ability of cells to proliferate indefinitely. The cells with this ability can form a large colony or a clone of cells which known as clonogenic cells. Various mechanisms are involved in cell death, however, the loss of cells ability in proliferation and propagation are known as the most common factor. So, the cells that remain the ability of proteins and DNA synthesis can go through one or two mitoses, but are unable to divide and produce a large number of population are known dead. The assay was considered for examination of treated cells with ZrP-MB nanostructures proliferation potential under laser illumination.

As can be seen in Fig. 8, the colony forming ability of the cells treated with various concentrations of ZrP-MB was decreased upon increasing the nanoparticle concentration in compare to control group (dark). It is clear that

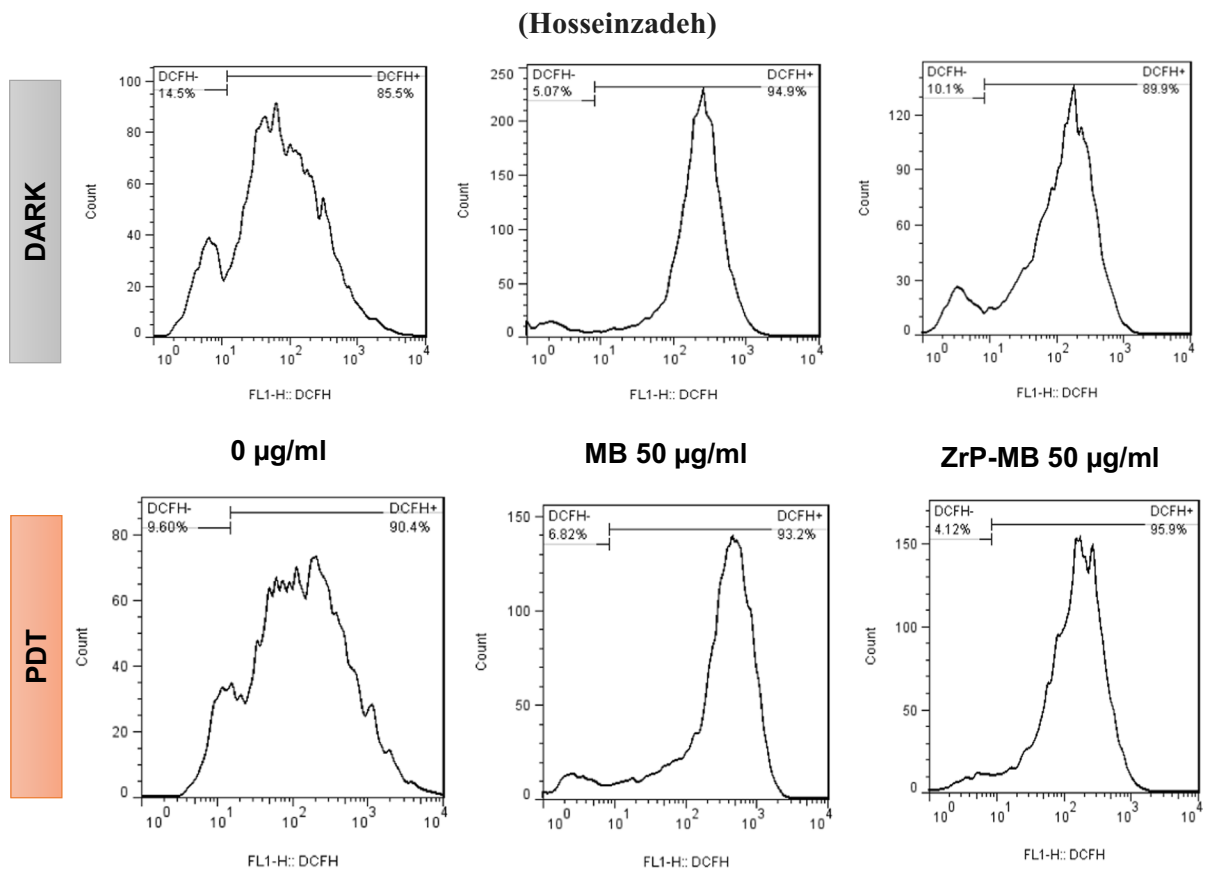


**Figure 10.** Effects of MB (50 µg/ml) and ZrP-MB (50 µg/ml) following PDT on intracellular ROS generation in MDA-MB-231 cells. The cells were stained with DCFH-DA (2 mM), followed by flow cytometry. DCFH-DA will be converted to DCFH<sup>+</sup> in presence of reactive oxygen species (ROS) and induce fluorescence signal in histogram.

the PDT treatment by synthesized hybrid ZrP-MB nanoparticles induced cell death and decreased proliferation ability of MDA-MB-231 breast cancer cells.

**Apoptosis detection: AO/EB double staining and flow cytometry.** To obtaining the apoptotic induction ability of ZrP-MB nanoparticles on MDA-MB-231 cancer cells, we treated the cells with (0, 10 and 50 µg/ml of ZrP-MB nanoparticle) and then PDT. The cells stained with Acridine Orange (AO) and Ethidium Bromide (EB) for fluorescence microscopy. Also the cells were stained with Annexin V-FITC and PI followed by flow cytometry analysis.

As it can be seen in Fig. 9, under a fluorescence microscope, the normal cells (control) are green and have intact and round-shape nuclei. After treatment with ZrP-MB nanoparticle then PDT the cells turned to red (early or late apoptotic cells) with condensed or fragmental nuclei. Late apoptotic and necrotic cells were increased upon increasing ZrP-MB nanoparticle concentration (10 to 50 µg/mL). Annexin V binding and PI uptake is one of the most commonly method in measurement of cellular apoptosis and necrosis. The asymmetry of membrane phospholipids is perturbed in apoptotic cells and the loss of membrane conformational asymmetry causes the releasing of phosphatidylserine on the outer side of the plasma membrane. Annexin V binding to externalized phosphatidylserine can be used in measurement of cellular apoptosis. Also, apoptotic cells are characterized by DNA fragmentation and, consequently, that can be determined by staining with Propidium Iodide (PI) and following by flow cytometry assay. According to the obtained flow cytometry histograms (Fig. 9) related to ZrP-MB treatment at various concentrations and then PDT, it is clear that the apoptotic and necrotic cells were increased by increasing ZrP-MB concentration. As shown in Figs 5 and 6, the control shows 4% apoptotic cells (Q2 and Q3) whereas after treatment with 10 and 50 µg/ml of ZrP-MB then PDT, the early apoptotic cells represented 10%, 13% (Q3) and late apoptotic cells represented 5% and 30% (Q2) of the total cells, respectively. At 50 µg/ml of ZrP-MB 7% necrosis is also observed (Q1). It can be concluded that by increasing nanoparticles concentration the apoptotic cells increased.

**ROS generation after PDT with ZrP-MB.** In PDT, the excited photosensitizer transfers energy to molecular oxygen and generates cytotoxic reactive oxygen species (ROS) which could induce oxidative damages or cell death<sup>60</sup>. However, it is not clear whether ROS generation is involved in cell death mechanism of ZrP-MB -PDT.

To clarify it, we examined intracellular ROS generation in terms of flow cytometry by DCFH-DA. As it can be seen in Fig. 10, at dark condition the ROS generation in cells, treated with MB, is higher than the cells treated with ZrP-MB. While after PDT the cells that treated with ZrP-MB displayed higher ROS generation compared to MB treated cells.

According to the obtained results and considering various scientific research reports, it can be concluded that the synthesized nano-hybrid materials can be used for selective photodynamic treatment of cancer cells, in the presence of normal cells, due to the selective release of methylene blue because of cation exchange ability of zirconium phosphate in the acidic microenvironment of cancer cells<sup>32–34,61</sup>. By exchanging methylene blue cations with hydrogen ions ( $H^+$ ), the releasing of methylene blue was occurred and photo-activation of MB using red light LED illumination caused photodynamic cell killing on cancer cells, consequently<sup>29,62</sup>.

## Conclusion

In conclusion, we have synthesized and characterized ZrP NPs, and then methylene blue was loaded in the inter-layer part of the nanoplatelets. The dark cytotoxicity experiments demonstrated that the synthesized nanoplatelets were biocompatible and didn't show any significant cytotoxicity. The drug loading fine efficacy, swelling and water dispersibility were the characteristics of obtained nanoparticles. ZrP-MB NPs were effective in delivery of the methylene blue to MDA-MB-231 breast cancer cells. Dark experiments clarified that methylene blue cellular toxicity decreased by intercalating into the layers of ZrP nanoparticles. Photodynamic therapy using synthesized nanoparticles demonstrated that the intercalation can enhance the PDT efficacy based on decreasing methylene blue dark toxicity and prevention of methylene blue environmental redox reactions. In the other words, it could be stated that the methylene blue intercalation in ZrP nanoparticles increased selectivity in local photodynamic toxicity based on selective laser illumination. According to the acidic extracellular microenvironment of cancer cells and considering the characteristics of ZrP nanoparticles cation exchange ability, selective release of methylene blue in the cancer cells microenvironment can enhance the photodynamic therapy efficacy. The clonogenic assay, fluorescence microscopic image and flow cytometry experiments of treated cells confirmed the obtained results. The lack of cytotoxicity of zirconium phosphate nanoplatelets offered promising potential in application of ZrP nanoparticles as cationic photosensitizer's carrier for effective photodynamic therapy. At the end, *in vivo* studies needed to evaluate the toxicity, feasibility and efficacy of ZrP-MB nanoparticles in breast cancer animal models.

## Data Availability

The datasets generated and analyzed during the current study are available from the corresponding authors on reasonable request by permission of institute and department chairmans.

## References

- Shahdordizadeh, M., Yazdian-Robati, R., Ramezani, M., Abnous, K. & Taghdisi, S. M. Aptamer application in targeted delivery systems for diagnosis and treatment of breast cancer. *J. Mater. Chem. B* **4**, 7766–7778 (2016).
- Wang, C. *et al.* Triple negative breast cancer in Asia: An insider's view. *Cancer Treat. Rev.* **62**, 29–38 (2018).
- Ahjum, F., Razvi, N. & Masood, M. A. Breast Cancer Therapy: A Mini Review. *MOJ Drug Des. Dev. Ther.* **1** (2017).
- Khorsandi, K., Hosseinzadeh, R. & Fateh, M. Curcumin intercalated layered double hydroxide nanohybrid as a potential drug delivery system for effective photodynamic therapy in human breast cancer cells. *RSC Adv.* **5** (2015).
- Lee, A. & Djamgoz, M. B. A. Triple negative breast cancer: Emerging therapeutic modalities and novel combination therapies. *Cancer Treat. Rev.* **62**, 110–122 (2018).
- Mouridsen, H. T., Palshof, T., Brahm, M. & Rahbek, I. Evaluation of single-drug versus multiple-drug chemotherapy in the treatment of advanced breast cancer. *Cancer Treat. Rep.* **61**, 47–50 (1977).
- Waldman, S. A. & Terzic, A. *Pharmacology and Therapeutics: Principles to Practice.* (Saunders/Elsevier, 2009).
- Johnson, N. P. *et al.* Metal Antitumor Compounds: The Mechanism of Action of Platinum Complexes. *Prog. Clin. Biochem. Med.* **10**, 1–24 (1989).
- Martin, M. *et al.* Carboplatin: an active drug in metastatic breast cancer. *J. Clin. Oncol.* **10**, 433–7 (1992).
- Perez, E. A. *et al.* Two concurrent phase II trials of paclitaxel/carboplatin/trastuzumab (weekly or every-3-week schedule) as first-line therapy in women with HER2-overexpressing metastatic breast cancer: NCCTG study 983252. *Clin. Breast Cancer* **6**, 425–32 (2005).
- Burch, P. A. *et al.* Phase II study of gemcitabine plus cisplatin in patients with metastatic breast cancer: a North Central Cancer Treatment Group Trial. *Am. J. Clin. Oncol.* **28**, 195–200 (2005).
- Blum, J. L. *et al.* Multicenter, Phase II study of capecitabine in taxane-pretreated metastatic breast carcinoma patients. *Cancer* **92**, 1759–68 (2001).
- Vu, T. & Claret, F. X. Trastuzumab: updated mechanisms of action and resistance in breast cancer. *Front. Oncol.* **2**, 62 (2012).
- Li, S. *et al.* Quercetin enhances chemotherapeutic effect of doxorubicin against human breast cancer cells while reducing toxic side effects of it. *Biomed. Pharmacother.* **100**, 441–447 (2018).
- Singh, K., Bhoori, M., Kasu, Y. A., Bhat, G. & Marar, T. Antioxidants as precision weapons in war against cancer chemotherapy induced toxicity – Exploring the armoury of obscurity. *Saudi Pharm. J.* **26**, 177–190 (2018).
- Tao, J. J., Visvanathan, K. & Wolff, A. C. Long term side effects of adjuvant chemotherapy in patients with early breast cancer. *The Breast* **24**, S149–S153 (2015).
- Liu, K., Jiang, X. & Hunziker, P. Carbohydrate-based amphiphilic nano delivery systems for cancer therapy. *Nanoscale* **8**, 16091–16156 (2016).
- Balaji, A. *et al.* An insight on electrospun-nanofibers-inspired modern drug delivery system in the treatment of deadly cancers. *RSC Adv.* **5**, 57984–58004 (2015).
- Karimi, M. *et al.* Smart micro/nanoparticles in stimulus-responsive drug/gene delivery systems. *Chem. Soc. Rev.* **45**, 1457–1501 (2016).
- Baek, S. *et al.* Smart multifunctional drug delivery towards anticancer therapy harmonized in mesoporous nanoparticles. *Nanoscale* **7**, 14191–14216 (2015).
- Mahmoodi, N. O., Ghavidast, A. & Amirmahani, N. A comparative study on the nanoparticles for improved drug delivery systems. *J. Photochem. Photobiol. B Biol.* **162**, 681–693 (2016).
- Aftab, S. *et al.* Nanomedicine: An effective tool in cancer therapy. *Int. J. Pharm.* **540**, 132–149 (2018).
- Singh, R. & Lillard, J. W. Nanoparticle-based targeted drug delivery. *Exp. Mol. Pathol.* **86**, 215–223 (2009).

24. Parveen, S., Misra, R. & Sahoo, S. K. Nanoparticles: a boon to drug delivery, therapeutics, diagnostics and imaging. *Nanomedicine Nanotechnology, Biol. Med.* **8**, 147–166 (2012).
25. Sahoo, S. K. & Labhasetwar, V. Nanotech approaches to drug delivery and imaging. *Drug Discov. Today* **8**, 1112–1120 (2003).
26. Brigger, I., Dubernet, C. & Couvreur, P. Nanoparticles in cancer therapy and diagnosis. *Adv. Drug Deliv. Rev.* **64**, 24–36 (2012).
27. Choy, J.-H., Kwak, S.-Y., Jeong, Y.-J. & Park, J.-S. Inorganic Layered Double Hydroxides as Nonviral Vectors. *Angew. Chemie* **39**, 4041–4045 (2000).
28. Bringley, J. F. & Liebert, N. B. Controlled Chemical and Drug Delivery via the Internal and External Surfaces of Layered Compounds. *J. Dispers. Sci. Technol.* **24**, 589–605 (2003).
29. Viseras, C., Cerezo, P., Sanchez, R., Salcedo, I. & Aguzzi, C. Current challenges in clay minerals for drug delivery. *Appl. Clay Sci.* **48**, 291–295 (2010).
30. Khorsandi, K., Hosseinzadeh, R. & Fateh, M. Curcumin intercalated layered double hydroxide nanohybrid as a potential drug delivery system for effective photodynamic therapy in human breast cancer cells. *RSC Adv.* **5**, 93987–93994 (2015).
31. Auerbach, S. M., Carrado, K. A. & Dutta, P. K. *Handbook of Layered Materials*. (CRC Press, 2004).
32. Saxena, V., Diaz, A., Clearfield, A., Batteas, J. D. & Hussain, M. D. Zirconium phosphate nanoplatelets: a biocompatible nanomaterial for drug delivery to cancer. *Nanoscale* **5**, 2328 (2013).
33. Diaz, A. *et al.* Zirconium phosphate nano-platelets: a novel platform for drug delivery in cancer therapy. *Chem. Commun.* **48**, 1754–1756 (2012).
34. Díaz, A. *et al.* Direct intercalation of cisplatin into zirconium phosphate nanoplatelets for potential cancer nanotherapy. *Nanoscale* **5**, 11456–63 (2013).
35. Yu, S. *et al.* Synthesis and Characterization of  $\alpha$ -ZrP@CHI Drug Deliver System. *J. Nanosci. Nanotechnol.* **16**, 3628–3631 (2016).
36. Trobajo, C., Khainakov, Sa, Espina, a & Garcia, J. R. On the synthesis of alpha-zirconium phosphate. *Chem. Mater.* **12**, 1787–1790 (2000).
37. Hosseinzadeh, R. & Khorsandi, K. Methylene blue, curcumin and ion pairing nanoparticles effects on photodynamic therapy of MDA-MB-231 breast cancer cell. *Photodiagnosis Photodyn. Ther.* **18** (2017).
38. Hosseinzadeh, R., Khorsandi, K. & Jahanshahi, M. Combination photodynamic therapy of human breast cancer using salicylic acid and methylene blue. *Spectrochim. Acta - Part A Mol. Biomol. Spectrosc.* **184**, 198–203 (2017).
39. Hosseinzadeh, R., Khorsandi, K. & Hosseinzadeh, G. Graphene oxide-methylene blue nanocomposite in photodynamic therapy of human breast cancer. *J. Biomol. Struct. Dyn.*, <https://doi.org/10.1080/07391102.2017.1345698> (2017).
40. Spring, B. Q., Rizvi, I., Xu, N. & Hasan, T. The role of photodynamic therapy in overcoming cancer drug resistance. *Photochem. Photobiol. Sci.* **14**, 1476–1491 (2015).
41. Lin, G., Mi, P., Chu, C., Zhang, J. & Liu, G. Inorganic Nanocarriers Overcoming Multidrug Resistance for Cancer Theranostics. *Adv. Sci.* **3**, 1600134 (2016).
42. Khadair, A. *et al.* Nanoparticle-mediated combination chemotherapy and photodynamic therapy overcomes tumor drug resistance. *J. Control. Release* **141**, 137–144 (2010).
43. Obaid, G. *et al.* Photonanomedicine: a convergence of photodynamic therapy and nanotechnology. *Nanoscale* **8**, 12471–12503 (2016).
44. Tardivo, J. P. *et al.* Methylene blue in photodynamic therapy: From basic mechanisms to clinical applications. *Photodiagnosis Photodyn. Ther.* **2**, 175–191 (2005).
45. Shuai, M., Mejia, A. F., Chang, Y.-W. & Cheng, Z. Hydrothermal synthesis of layered  $\alpha$ -zirconium phosphate disks: control of aspect ratio and polydispersity for nano-architecture. *CrystEngComm* **15**, 1970 (2013).
46. Zhang, X. *et al.* Hydrothermal Synthesis of Copper Zirconium Phosphate Hydrate [Cu(OH)<sub>2</sub>Zr(HPO<sub>4</sub>)<sub>2</sub>·2H<sub>2</sub>O] and an Investigation of its Lubrication Properties in Grease. *ACS Appl. Mater. Interfaces* **5**, 7989–7994 (2013).
47. Rafehi, H. *et al.* Clonogenic Assay: Adherent Cells. *J. Vis. Exp.*, <https://doi.org/10.3791/2573> (2011).
48. Olsen, C. E. *et al.* Development of resistance to photodynamic therapy (PDT) in human breast cancer cells is photosensitizer-dependent: Possible mechanisms and approaches for overcoming PDT-resistance. *Biochem. Pharmacol.* **144**, 63–77 (2017).
49. Nonaka, T. *et al.* Analysis of apoptotic effects induced by photodynamic therapy in a human biliary cancer cell line. *Anticancer Res.* **30**, 2113–2118 (2010).
50. Crowley, L. C., Marfèll, B. J., Scott, A. P. & Waterhouse, N. J. Quantitation of apoptosis and necrosis by annexin V binding, propidium iodide uptake, and flow cytometry. *Cold Spring Harb. Protoc.* **2016**, 953–957 (2016).
51. Xia, F., Yong, H., Han, X. & Sun, D. Small Molecule-Assisted Exfoliation of Layered Zirconium Phosphate Nanoplatelets by Ionic Liquids. *Nanoscale Res. Lett.* **11**, 348 (2016).
52. Grattan-Bellew, P. E. Petrographic and Technological Methods for Evaluation of Concrete Aggregates. In *Handbook of Analytical Techniques in Concrete Science and Technology* 63–104 (Elsevier, 2001).
53. dos Santos, A. F. *et al.* Methylene blue photodynamic therapy induces selective and massive cell death in human breast cancer cells. *BMC Cancer* **17**, 194 (2017).
54. Halliwell, B. Antioxidants in Human Health and Disease. *Annu. Rev. Nutr.* **16**, 33–50 (1996).
55. Kumari, S., Badana, A. K., G. M. M., G. S. & Malla, R. Reactive Oxygen Species: A Key Constituent in Cancer Survival. *Biomark. Insights* **13**, 117727191875539 (2018).
56. Ježek, J., Cooper, K. & Strich, R. Reactive Oxygen Species and Mitochondrial Dynamics: The Yin and Yang of Mitochondrial Dysfunction and Cancer Progression. *Antioxidants* **7**, 13 (2018).
57. Barrera, G. *et al.* Mitochondrial Dysfunction in Cancer and Neurodegenerative Diseases: Spotlight on Fatty Acid Oxidation and Lipoperoxidation Products. *Antioxidants* **5**, 7 (2016).
58. Zahedi, A. *et al.* Deep Analysis of Mitochondria and Cell Health Using Machine Learning. *Sci. Rep.* **8**, 16354 (2018).
59. Ma, D. *et al.* Cancer Cell Mitochondria Targeting by Pancreatistatin Analogs is Dependent on Functional Complex II and III. *Sci. Rep.* **7**, 42957 (2017).
60. Wang, W., Moriyama, L. T. & Bagnato, V. S. Photodynamic therapy induced vascular damage: an overview of experimental PDT. *Laser Phys. Lett.* **10**, 23001 (2013).
61. Kalita, H. *et al.* Sonochemically synthesized biocompatible zirconium phosphate nanoparticles for pH sensitive drug delivery application. *Mater. Sci. Eng. C* **60**, 84–91 (2016).
62. González, M. L. *et al.* Zirconium Phosphate Nanoplatelet Potential for Anticancer Drug Delivery Applications. *J. Nanosci. Nanotechnol.* **16**, 117–129 (2016).

## Acknowledgements

The authors gratefully acknowledge all peoples who help us to do this project. We are thankful for instrumental supports of our work by academic center for education, culture and research.

## Author Contributions

R.H. designed and performed synthesis, characterization experiments of nanoparticles and drafted the manuscript. K.K. Performed cellular experiments, analyzed results and revised the manuscript.

## Additional Information

**Competing Interests:** The authors declare no competing interests.

**Publisher's note** Springer Nature remains neutral with regard to jurisdictional claims in published maps and institutional affiliations.



**Open Access** This article is licensed under a Creative Commons Attribution 4.0 International License, which permits use, sharing, adaptation, distribution and reproduction in any medium or format, as long as you give appropriate credit to the original author(s) and the source, provide a link to the Creative Commons license, and indicate if changes were made. The images or other third party material in this article are included in the article's Creative Commons license, unless indicated otherwise in a credit line to the material. If material is not included in the article's Creative Commons license and your intended use is not permitted by statutory regulation or exceeds the permitted use, you will need to obtain permission directly from the copyright holder. To view a copy of this license, visit <http://creativecommons.org/licenses/by/4.0/>.

© The Author(s) 2019